Solar-Light Photoamperometric and Photocatalytic Properties of Quasi-transparent TiO_2 Nanoporous Thin Films

Yajun Ji,[†,‡] Keng-Chu Lin,[†,§] Hegen Zheng,[‡] Chung-Chiun Liu,[⊥] Laurie Dudik,[⊥] Junjie Zhu,*[,‡] and Clemens Burda*[,†,§]

Chemistry Department, Department of Chemical Engineering, and Department of Material Science and Engineering, Case Western Reserve University, 10900 Euclid Avenue Cleveland, Ohio 44106, United States, and Key Laboratory of Analytical Chemistry for Life Science, Department of Chemistry, Nanjing University, Nanjing 210093, P. R. China

ABSTRACT Transparent photocatalytic surfaces are of ever increasing importance for many applications on self-cleaning windows and tiles in everyday applications. Here, we report the formation and photocatalytic testing of a quasi-transparent thin and nanoporous titania films deposited on glass plates. Sputtered Ti thin films were anodized in fluoride-ion-containing neutral electrolytes to form optically semitransparent nanoporous films, which transformed to be completely transparent after thermal annealing. The nanoporous films were studied at different stages, such as before and after anodization, as well as after thermal annealing using scanning electron microscopy (SEM), X-ray diffraction (XRD), and UV−vis and Raman spectroscopy. It was observed that anodization at 20 V of high-temperature deposited titanium films resulted in regular nanopore films with pore diameters of 30 nm. Structural investigations on the transparent nanopore arrays reveal the presence of anatase phase TiO_2 even after annealing at 500 °C, which was confirmed by XRD and Raman spectroscopy measurements. The solar-light induced photocatalytic decomposition of stearic acid and photoconductivity characteristics of these nanoporous thin films are also presented.

KEYWORDS: titania nanopores • thin film • photocurrent • photocatalysis

1. INTRODUCTION

The discovery of photocatalytic water splitting on TiO_2 two decades ago by Honda and Fujishima (1) generated a field of extensive research with wide ranging potential (2). The photocatalytic properties of TiO_2 have been tested in organic synthesis (3), environmental cleanup (4), antibacterial (5), and self-cleaning (6) applications. Besides the excellent photocatalytic performance, TiO_2 also has found multiple applications in hydrogen sensors (7), electrochromic devices (8), biomedicine (9), and solar energy conversion (10) because of its remarkable physical and chemical properties. It is well-known that the properties and performance of TiO_2 partly depend on its crystallinity and morphology (11). Especially, TiO_2 nanotubes are currently under intense investigation, as they provide highly active surfaces with a large surface to volume ratio and a unidirectional electrical channel compared to TiO_2 nanoparticle-based films (12−14).

Sol−gels (15, 16), sonochemistry (17), anodization (11), and surfactant templating (18) approaches have been used to fabricate nanotubular structures of which anodization are one of the most promising routes. In this report, Ti, in the form of a film or foil, is anodized in fluoride-ion-containing electrolytes to form nanopores/tubes. The first porous oxide layers were anodically grown on Ti metal in 1999 (19). After that Grimes et al. obtained TiO_2 nanotubes by the anodization of a pure Ti sheet in an aqueous solution of hydrofluoric (HF) acid in 2001 (20). From then on significant progress has been made in this field (21, 22). The nanotube-array length was subsequently increased from 500 nm to 7 μm by control of the anodization electrolyte pH, which reduced the chemical dissolution of TiO_2 during the anodization (23). More recently, a new generation of vertically oriented TiO_2 nanotubes with lengths of up to 134 μm has been fabricated by the use of organic electrolytes (22). In addition, Bamboo-type tubes were prepared electrochemically by controlled anodization of Ti foil in an electrolyte consisting of 0.2 mol L^{-1} HF in ethylene glycol under specifically controlled alternating-voltage conditions (24).

In order to get TiO_2 nanotube arrays with large surface area, which are defect free, and have perfect alignment, the Grimes and Schmuki groups have conducted comprehensive studies on Ti foil anodization (16, 23). In their published work, the effect of the electrochemical sweep rate, the electrolyte concentration, applied voltage, oxidation time as well as other important factors on the pore structure were investigated in detail. More recently, the effect of electrolyte temperature on the formation of highly ordered TiO_2 nanotube arrays has also been investigated by Zhou's group (25). However, the fabrication of these nanotube arrays from a starting Ti foil, which underlies the nanotube array, can limit

* Corresponding author. E-mail: burda@case.edu.
Received for review July 2, 2010 and accepted October 7, 2010
† Chemistry Department, Case Western Reserve University.
‡ Nanjing University.
§ Department of Material Science and Engineering, Case Western Reserve University.
⊥ Department of Chemical Engineering, Case Western Reserve University.
DOI: 10.1021/am100579g

their potential applications, particularly in the fabrication of microscale devices. Therefore, several research groups have developed alternative methods for the fabrication of nanoporous TiO_2 via the anodization of titanium films (26−30). Mor et al. (27, 31) first reported the anodization of Ti-metal thin films to obtain nanotube arrays in an electrolyte containing acetic acid and hydrofluoric acid. The diameter of the obtained nanotube arrays was in the range of 30−50 nm.

Anodization of thin films is a much less well-known process than from foils due to its specific complications. During the process of anodization, there are two factors that should be focused on: (i) usually, an initiation phase with disordered oxide growth occurs before self-ordering is established. (ii) In many electrolytes, anodization is accompanied by significant TiO_2 losses due to competing chemical dissolution. In addition, the deposition temperature, the stress mismatch of the substrate and Ti films, the thickness of the films, and the type of deposition all affect the films which in return affect the anodization process (32). Recently, highly ordered transparent TiO_2 nanotube arrays on conductive glass substrates had been successfully used in electrochromic devices (33) and dye-sensitized solar cells (31, 34). Herein, we focus on their photocatalytic performance. Thousand nanometer Ti-coated fluorine-doped tin oxide (FTO)-coated glasses were used for the anodization process. Under constant applied voltage, a high-purity Ti thin film was electrochemically anodized in nonaqueous electrolytes. The study showed that TiO_2 nanopore structures had formed with optically transparent appearance. The optical properties of the nanopore structures have been investigated. The as-prepared TiO_2 nanopore structures were amorphous and converted into anatase phase via high temperature annealing at 500 °C; the crystalline transformation was studied by XRD and Raman spectroscopy measurements. Then, the photocatalytic decomposition of stearic acid and photoconductivity behaviors of these obtained electrodes was investigated. To the best of our knowledge, this is the first report of the photocatalytic performance of quasi-transparent TiO_2 nanopores electrodes.

2. EXPERIMENTAL SECTION

2.1. Preparation. ***Sputtering.*** For this study, titanium films of 1000 nm thickness were first deposited onto FTO glass substrates using the RF sputtering technique from a 99.99% pure Ti target. RF power of 250 W was applied during the deposition process. The sputtering chamber was pumped down to the background pressure of 4.0×10^{-7} Torr before introducing the sputtering gas of 100% Ar with a pressure of 2×10^{-3} Torr. The substrate temperature was 200 °C. Based on the known sputtering rate and the adjusted deposition time, 1000 nm thick titanium films were obtained and each coating film thickness was measured with a laser profile scanner (OGP Cobra, Rochester, NY) to confirm the film thickness.

Anodization. Prior to electrochemical treatment the sputtered samples were sonicated in alcohol and distilled water for 10 min each. Then they were dried in air. Anodization was performed in a neutral electrolyte medium of 0.25 wt % NH_4F/ethylene glycol solutions using a platinum foil cathode at room temperature and atmospheric pressure. Nanoporous structures were grown on Ti thin films using an anodizing potential of 20 V without stirring. The sputtered samples turned to semitransparent after several hours anodization, then the reaction stopped. The geometry of the cell is schematically shown in Figure 1. After anodization, the samples were cleaned with deionized water and then dried under forced air. Finally, the as-prepared amorphous TiO_2 thin films were annealed at 500 °C for 2 h. Heating and cooling rates were 2 °C min^{-1}.

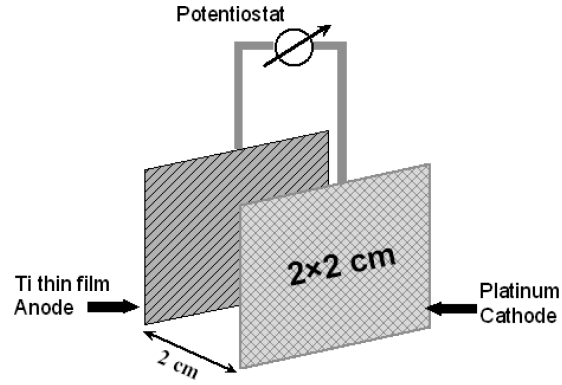

FIGURE 1. Schematic drawing of an electrochemical cell in which the Ti thin film coated on FTO glass is anodized. The distance between anode and cathode is kept at 2 cm. The voltage was kept at 20 V.

Film Characterization. The morphology of the annealed TiO_2 thin film was characterized using a field emission scanning electron microscope (S4500 Hitachi). Five kV accelerating voltage was typically used to record the images. The chemical composition was determined by energy dispersive X-ray analysis (EDX). X-ray diffraction (XRD) patterns were obtained for the nanocrystal sample using a Philips PW 3710 X-ray powder diffractometer. The crystalline nature of both prepared and annealed TiO_2 nanotube arrays were examined using a Thermoelectron Nexus Raman spectrometer equipped with a diode laser (972 nm wavelength). The UV−vis transmission spectra of the nanocrystal samples were measured on a Cary 50 UV−visible spectrometer. The FTIR spectra were obtained with a Nexus 870. All measurements were carried out at room temperature.

2.2. Photocatalytic Activity Measurement. High-molecular-weight organic molecules, namely stearic acid, were coated dropwise onto the transparent TiO_2 nanopore electrode from 0.02 M stearic acid in methanol. The organic coated nanopore electrode was irradiated by an arc Xenon lamp. The Xenon lamp output was fixed to 150 W. The organic film-coated nanopore electrode was fixed on the FTIR sample holder, which allowed the light to pass through a 1.6 cm^2 opening window to the sample. The irradiation of Xenon lamp onto the sample was fixed to 100 mW/cm^2. The electrode was affixed to the FTIR sample holder during irradiation and IR spectral acquisition to ensure the measurement was on the identical area as was irradiated. Irradiation and IR measurement were performed at room temperature. The photodegradation of organic molecules was quantitatively determined by monitoring the decreasing of C−H peak area in 2700−3000 cm^{-1} range from FTIR spectra.

2.3. Photoconductivity. The photoconductivity was determined as a function of time and measured under modulated irradiation conditions under different atmospheres at room temperature. The measurement was carried out in coplanar configuration (copper contacts with a distance between them 0.5 mm). A constant voltage 15 V was applied to the samples by a Keithley 2400 sourcemeter. The irradiation by the Xenon lamp with an AM1.5 and a water heat filter was adjusted to 100 mW/cm^2. The light was switched on and off every 2 min alternating and the corresponding photocurrent response.

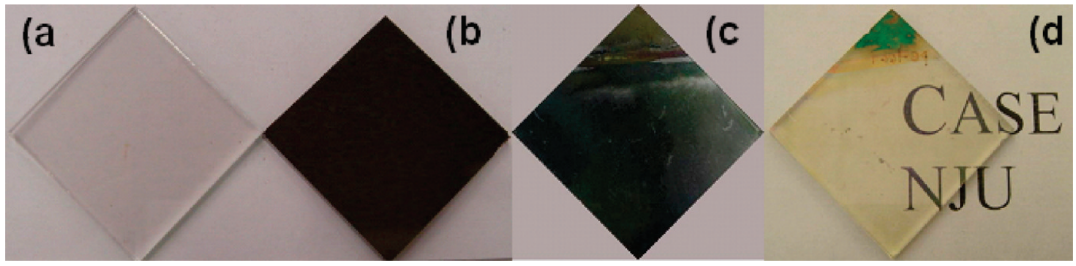

FIGURE 2. Digital images of (a) FTO on a glass substrate, (b) Ti coated on FTO/glass before anodization, (c) after anodization, and (d) after thermal annealing. The text "CASE, NJU" is written underneath on paper to demonstrate the degree of transparency.

3. RESULTS

3.1. TiO_2 Nanopore Structures Obtained from Nonaqueous Electrolytes. As discussed in previous studies, the sputtering conditions play an important role on the quality of the sputtered Ti layer (32, 33). High-temperature sputtered films result in the formation of well-ordered nanotubes. Whereas, randomly oriented nanopores and short tubes were observed within grain boundaries for room-temperature sputterred films (28). Therefore, the sputtered samples in our work were prepared under high temperature deposition. Deposited films were found to have good adhesion to the substrate and were also observed to remain stable when immersed in the electrolyte. The digital images in Figure 2 show (a) the FTO glass substrate, (b) the Ti coated FTO glass before anodization, (c) after anodization, and (d) after thermal annealing. Initially, the Ti-coated glass was dark. After several hours of anodization, the anodized area became semitransparent; upon subsequent thermal annealing at 500 °C, the anodized area changed to be optically transparent with a light yellow hue.

The morphologies of the corresponding samples were characterized by FE-SEM. The microstructures of FTO glass and Ti films of thickness ~1000 nm deposited at 200 °C are shown in Figure 3a,b. As can be seen in Figure 3a, there is large surface area of fluorine-doped SnO_2 particles on the glass surface. After sputtering, the films had a closely packed granular titanium structure.

To better understand the anodization process, the SEM of a sputtered sample after 10 min anodization had also been investigated. One can see that holes are formed on the Ti surface (Figure 3c), as the anodization continues, which is due to the presence of fluoride ions. As the process continues, these holes become larger and the metal oxide barrier layer starts to peel off. When the thin film showed semitransparent appearance, the anodization process was stopped. After thermal annealing, the semitransparent appearance was transformed to complete transparency.

Mor et al. (27) and Yang et al. (29, 35) have reported the presence of well-ordered nanotubes on films sputtered at high temperatures (500 °C). Macak et al. (28) also obtained well-ordered nanotubes in ion-beam sputtered films, which were obtained at room temperature and low deposition pressure of 1×10^{-4} Torr. However, rather than nanotube arrays, a nanoporous TiO_2 film with thicker walls after thermal annealing was observed in our work as shown in Figure 3c,d. More recently, Kalantar's group found that the crystallographic orientation of the Ti films played a significant role in determining whether pores or tubes were formed during the anodic etching process (36). The inset higher-magnification SEM image in Figure 3d shows the obtained nanopores had an average diameter of 30 nm. The formation of TiO_2 after thermal annealing was demonstrated by the elemental signature in the EDX spectrum (Figure 3e). The EDX spectrum exhibits O, Sn, and Ti peaks, showing the presence of tin element, which was derived from the FTO substrate and the atomic percentage of Sn is 1.4%.

For the anodization of Ti foils, the applied voltage plays an important role in controlling the tube size. On average, the higher the voltage, the larger the diameter of the tubes is. The diameter of the nanoporous structure in this work is similar to that of nanotubes reported by Lin et al. (30). The formation of nanoporous films may be due to the short anodization time, which was limited by the original Ti film thickness predeposited. With a short anodization time, the etching speed of TiO_2 in nonaqueous electrolyte reduced and the self-organization process led to the finally observed nanoporous structure. In addition, the quality of the Ti films is critical to obtain highly ordered TiO_2 nanotube arrays (27, 31). An investigation into the sputtering conditions which produce smoother Ti thin films is underway. The anodized semitransparent samples showed the same nanoporous structure, which means that the nanoporous structures were retained after high-temperature annealing.

UV−vis transmission spectra of the original FTO on glass substrate, titanium films deposited on FTO glass, semitransparent Ti thin film after anodization and transparent nanoporous structure after thermal annealing are shown in Figure 4. The 1000 nm thick puttered film was first anodized at 20 V, and then it was annealed at 500 °C for 2 h in air. One can see that the anodized Ti thin film (c) showed low transmittance through the entire visible range. After annealing, the semitransparent sample became transparent (d) to the eye, with average absorbance of 0.3 throughout the visible range. Consequently, a higher transmittance was observed. However, as for titanium films deposited on FTO glass, there is no transmittance throughout the entire visible range. As can be seen, there is sharp decline in transmittance for wavelengths of less than 400 nm in curve d, which is due to the presence of TiO_2. For comparison, the transmittance spectrum of the FTO glass substrate is also shown (a).

3.2. Crystal Formation in TiO_2 Nanopore Arrays. ***XRD Spectra.*** After anodization, the obtained sample is brownish in color and has poor transparency. This

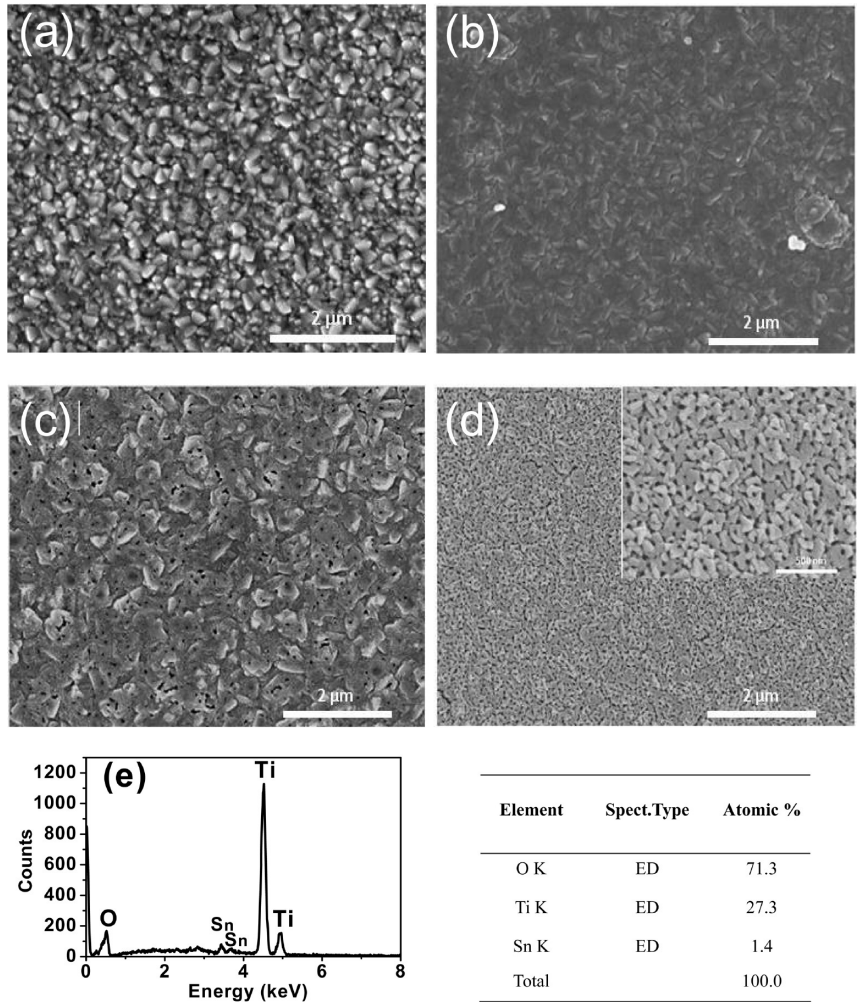

Element	Spect.Type	Atomic %
O K	ED	71.3
Ti K	ED	27.3
Sn K	ED	1.4
Total		100.0

FIGURE 3. Morphology of (a) bare FTO on glass, (b) titanium films deposited on FTO/glass, (c) sputtered film at 20 V anodization after 10 min, and (d) uniformly transparent TiO_2 nanopores structure prepared on FTO glass after thermal annealing. A higher magnification image of the microstructure is shown in the inset. (e) The corresponding EDX pattern of the TiO_2 nanopore film on FTO glass.

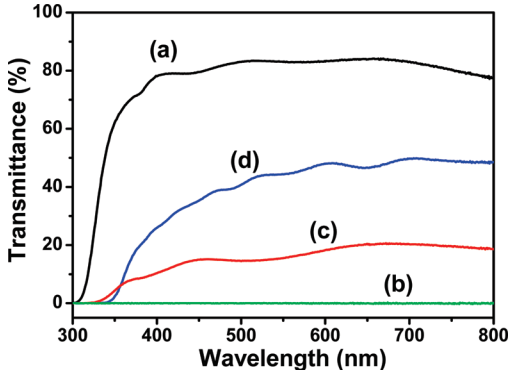

FIGURE 4. Transmittance spectra of (a) FTO/glass, (b) titanium films deposited on FTO/glass, (c) quasi-transparent Ti thin film after anodization, and (d) 500 °C annealed TiO_2 nanoporous structure on FTO glass.

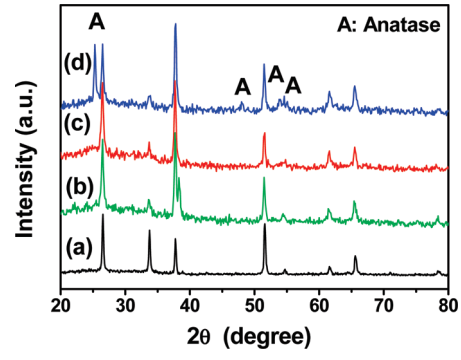

FIGURE 5. XRD patterns of (a) bare FTO on glass, (b) a titanium film deposited on FTO/glass, (c) a semitransparent Ti/TiO_2 thin film before thermal annealing, and (d) 500 °C annealed TiO_2 nanoporous structure on FTO glass. The peak at 38° in green trace (b) is due to Ti metal.

can be attributed to residue of metallic titanium still present underneath the nanotubular layer. To fully convert the layer to TiO_2 and to achieve a defined crystalline structure, subsequent heat treatment was performed (37). X-ray diffraction (XRD) patterns were used to characterize the atomic structure of the thin films before and after sintering. As shown in Figure 5, the semitransparent Ti/TiO_2 thin film after anodization was amorphous, and only diffraction peaks of FTO glass could be found. Clearly, after the annealing treatment at 500 °C for 2 h in air, the amorphous layer was completely transformed into an anatase structure (JCPDS file 84−1286) whereas all of the other peaks could be related to the remaining FTO coating. By comparing curves b and c, one can see that the peak scattered at 38° disappeared, which indicates that the sputtered Ti thin film had been

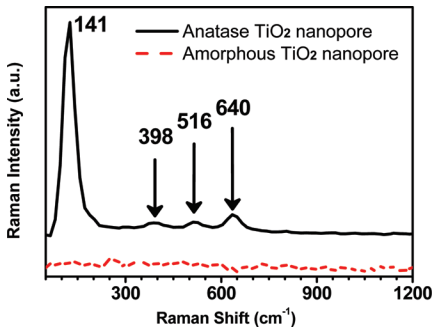

FIGURE 6. Raman spectra of amorphous (red dashed curve) and anatase (black solid curve) TiO_2 nanopores. After annealing at 500 °C for 2 h, amorphous TiO_2 was transformed into the anatase phase.

consumed after anodization. It has been reported in the literature (27, 38), the nanotubular surfaces would transform into rutile after annealing at elevated temperatures in the presence of oxygen. However, in our work, the sintered thin film shows mainly anatase structure.

Raman Spectroscopy. Figure 6 shows the Raman spectra taken for the titania nanopore samples before and after annealing. Ti−O−Ti signals in the 400−700 cm^{-1} range are characteristic of anatase and rutile structures (39). Typically, there are six Raman active fundamental modes observed at 144 cm^{-1} (E_g), 197 cm^{-1} (E_g), 397 cm^{-1} (B_{1g}), 518 cm^{-1} (A_{1g} + B_{1g}) and 640 cm^{-1} (E_g) for anatase TiO_2. For rutile TiO_2, there are four Raman active modes at 144 cm^{-1} (B_{1g}), 448 cm^{-1} (E_g), 613 cm^{-1} (A_{1g}), and 827 cm^{-1} (B_{2g}), respectively (40).

The TiO_2 nanopore structure obtained directly after anodization was amorphous, as revealed by Raman spectroscopy, for which a broad-band spectrum ranging from 100 to 1200 cm^{-1} is evident (red dashed curve in Figure 6). After thermal annealing, the amorphous TiO_2 nanopore structures were converted into the photoactive anatase phase. The annealed TiO_2 nanopores displayed Raman signals at 398, 516, and 640 cm^{-1}, which can be attributed to the phonon modes of the anatase phase (41, 42).

3.3. Photoconductivity of the Transparent TiO_2 Nanopore Arrays. Photoconductivity of TiO_2 films has a clear relationship with photocatalytic activity owing to the photogenerated carriers are the photoactive species (43, 44). In this work, the photoconductivity of the obtained nanopore arrays was also investigated. The plot of photoconductivity versus time of the samples measured in air and in argon during an on−off illumination cycle is shown in Figures 7 and 8, respectively. The photoconductivity behaviors of the nanopore electrodes with and without thermal annealing are shown in Figure 8. Two irradiation periods, each 2 min, were separated by the same period in darkness. An intensity of white light was kept constant at 100 mW/cm^2 (1 sun) for the illumination period during the measurement. The results presented in Figure 7 show that the photoconductivity of the nanopore electrode after the thermal annealing process was 2 orders of magnitudes higher than that without annealing. Without the heat annealing process, the TiO_2 nanopore layer remained amorphous. Even though this layer had a photoabsorbance in the UV portion of the white light, the noncrystalline TiO_2 structure hindered the photoinduced electron transport and led to extremely low photoconductivity. The photoconductivity of the sample with thermal annealing rose abruptly to a maximum and kept stable for 2 min then fell down to a steady state, which was well-reproducible for several hours.

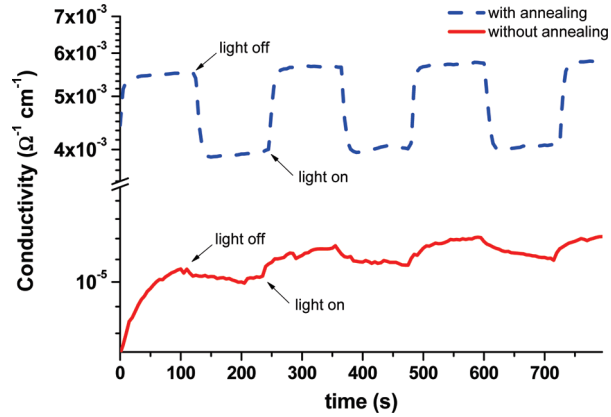

FIGURE 7. Photoconductivity of TiO_2 nanopore electrode with and without annealing versus time measured at room temperature in air.

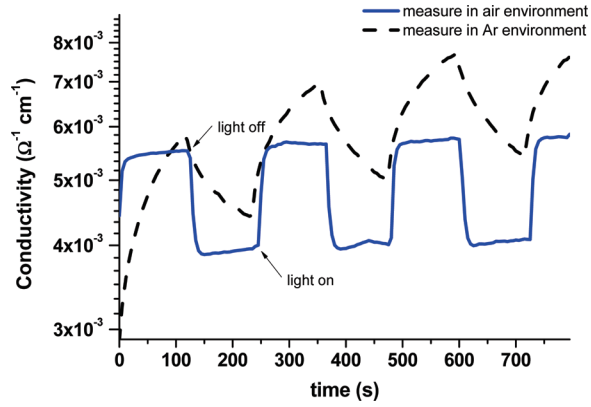

FIGURE 8. Photoconductivity of anatase TiO_2 nanopore electrodes versus time measured at room temperature under air and under argon atmosphere.

The photoconductivity behavior of anatase TiO_2 nanopore electrodes in air and in argon are shown in Figure 8. It was noticed that the photoconductivity is extremely sensitive to the ambient conditions. In argon the increase is slow, and the saturation of photocurrent is not attained even after two minutes of illumination. After the same time of illumination the average photoconductivity in argon is obviously larger than in air. The relatively low photoconductivity in air comparing to that in argon is attributed to the adsorbed O_2, which acts as a scavenger of photogenerated electrons. The adsorbed O_2 tends to trap the electrons because of its strong electronegativity to produce O^{2-} ions (45, 46). However, in argon atmosphere, the reduced concentration of O_2 reduces the electron removal rate and a much larger photocurrent is observed. The obtained photoconductivity results above show similar behavior as previous reports (47, 48).

3.4. Solar Photocatalysis with Stearic Acid. The photocatalytic degradation of stearic acid on the surface of transparent TiO_2 nanopore electrode is shown in Figure 9. Stearic acid, a high-molecular-weight compound, is often

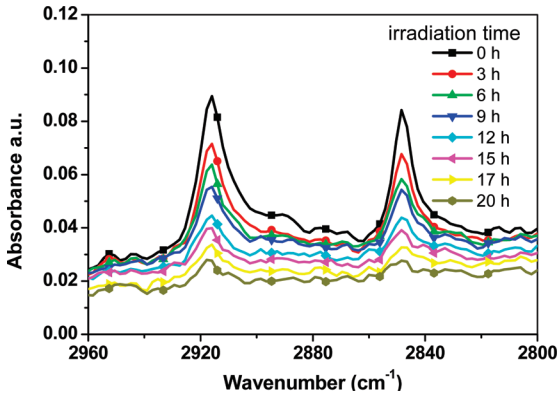

FIGURE 9. FTIR spectra of stearic-acid-coated transparent TiO_2 nanopore electrode as a function of irradiation time with a xenon lamp light using an AM1.5 and a water heat filter.

used as a model pollutant to probe photocatalytic activity. FTIR spectroscopy was employed to monitor the decomposition of stearic acid. The asymmetric and symmetric C−H stretching modes of the CH_2 group at 2915 and 2848 cm^{-1} were monitored as a function of irradiation time. A decrease in C−H stretch peak height indicates the removal of stearic acid from the surface (49).

From Figure 9, one can see that the CH_2 stretch peaks at 2,848 and 2,915 cm^{-1} decrease in intensity with increasing exposure time to the light. The decrease in area beneath the CH_2 stretch peaks measures the disappearance of stearic acid due to photocatalytic degradation. By comparing the number of the C−H stretch peaks at different stages, it can be observed that the photocatalytic decomposition rate at initial stage is higher than that of stage at longer irradiation times. After 20 h of irradiation, the stearic acid decomposition had basically been finished. All the photocatalytic decomposition tests are exposed to the full spectrum from the Xenon lamp with an AM1.5 and a water heat filter. These results presented the titania nanopore electrodes had a remarkable photocatalytic activity under the simulated solar spectrum.

4. DISCUSSION

4.1. Principle of the Thin Film Anodization Process. The synthetic process of the TiO_2 nanotube arrays and the mechanism of anodization had already been investigated in detail (32). Mor et al. (50) suggested that Ti anodization occurs as a result of a competition between electrochemical oxide formation and chemical dissolution of oxide by fluoride ions. For anodization, the Ti films should be placed in a conductive electrolyte along with a counter electrode. The growth process of nanotubes experiences three main stages. First, under constant-voltage conditions, a compact oxide layer forms that hampers further ion transfer corresponding to the electrochemical anodization.

In the second stage, the layer is partially perforated by fluoride ions accompanying an oxide dissolution (51), a fine porous layer forms. This means that the chemical dissolution will drive the electrochemical oxide formation. During the process, the fluoride anion is consumed, which is the key in controlling the surface morphology.

In the third stage, the situation is stabilized; the rate of titanium oxide growth assisted by the electric field equals the rate of dissolution by fluoride ions. Thus, regularly growing pores or tubes are formed. In addition, these growth stages have a close relationship to the current response under constant-voltage conditions. Close monitoring of the electric current response during potentiostatic anodization helped us to determine the optimum anodization parameters (27).

4.2. Photoconductivity Performance. The concentration of adsorbed oxygen at the electrode surface significantly affected the photoconductivity of the titania nanostructures. The titania nanopore electrode has a strong sensitivity to ambient conditions, which may arise from its increased surface to volume ratio. In argon atmosphere, the reduced concentration of absorbed O_2 reduced the electron trapping rate and extended the electron lifetime resulting in a higher saturation photocurrent. In terms of photoconductivity curve, during an on−off cycle, in air the photocurrent reaches a maximum rapidly and settles to the steady-state, and successive cycles of irradiation show an equal result. A similar photoconductivity behavior was observed in titania nanoparticulate films prepared by the colloid method (45). On the other hand, in argon the photocurrent rose slowly and we observed a tendency of increasing current in successive cycles, which is due to the low electron trap (adsorbed oxygen) concentration on the electrode surface.

4.3. Mechanism of the Photocatalytic Decomposition of Stearic Acid. Recently, the photocatalytic degradation of solid surface deposition such as fatty acids is of practical interest because they provide a reasonable model for the type of organics that deposit on an indoor (windows, tiles) or outdoor (walls, light covers) surface (52). In our work, the principle of photocatalytic decomposition of stearic acid can be summarized as follows (53).

Electrons are excited from the valence band to the conduction band in TiO_2 thin films when the transparent TiO_2 nanopore electrode is illuminated by sunlight, which gives rise to electron−hole pairs. The surviving electrons can react with O_2 to produce superoxide ions or with water to produce hydroxyl radicals. The generated radicals then participate in the decomposition of stearic acid. The corresponding reaction could be depicted as follows

$$\text{stearic acid} + 26\ O_2 \xrightarrow[\text{catalyst}]{h\nu \geq \text{band gap energy}} 18\ CO_2 + 18\ H_2O$$

4.4. Correlation of the Photoconductivity and Photodegradation. The photoconductivity of the titania nanopore electrode could be determined by two major factors: the quantity of the photoinduced electrons and holes, and the transport properties of the formed free carriers, which strongly depended on the degree of crystallinity, interfaces, and trapping sites in the nanostructures. In general, the photoconductive properties are based on the sum of the photogenerated carriers in the thin film and it

mainly is dominated by the net diffusion rates of the electrons and holes. For a highly efficient photodegradation of pollutants, sufficient photogenerated free carriers need to diffuse to the surface to react with oxygen or water. According to the photoconductivity experiments in Figures 7 and 8, the amorphous titania nanopore electrodes exhibited a very low photocurrent response resulting from the disordered structure. Hence, the photodegradation efficiency by using an unannealed amorphous titania nanopore electrode as photocatalyst was poor and could not be measured (results not shown). On the contrary, the crystalline anatase titania nanopore electrode produced by annealing presented noticeable photodecomposition, as shown in Figure 9.

4.5. Advantage of the Obtained Transparent TiO_2 Nanoporous Electrode. As self-cleaning coating, transparent TiO_2 nanopore electrodes had been obtained by direct anodization of Ti thin films. It avoided tedious procedures to coat TiO_2 nanoparticles on cleaned glass slides, as reported by previous work (6). In addition, the obtained transparent electrodes with ordered nanopore structure provide a larger contact area for high molecular organic pollutants than a nanosphere substrate. This is also beneficial to the charge transfer between the TiO_2 catalyst and the organic pollutants. Because of the presence of anatase crystals on the surface, the transparent TiO_2 nanopore electrode can mostly absorb the sun light with sacrificing some transmittance compared to that of the original FTO glass. On the basis of these presented properties, the transparent TiO_2 nanopore electrode could have applications in the future.

5. CONCLUSION

High-purity titanium thin films, deposited onto fluorine-doped tin oxide (FTO)-coated glass substrates, yielded a well-defined and regular nanopore anatase structure upon anodization in nonaqueous electrolytes under a constant applied voltage of 20 V. The TiO_2 nanostructures were examined by FE-SEM. The obtained nanoporous film had an average pore diameter of 30 nm. The study showed that optically transparent titania nanopore structures were obtained after thermal annealing. The corresponding optical transmittance spectra were investigated. After thermal annealing, the transmittance of the TiO_2 nanopore structures increased systematically. High temperature annealing of the TiO_2 nanopore structure induced the formation of the anatase phase, which was confirmed by XRD and Raman scattering measurements. In addition, the photocatalytic activity of the transparent TiO_2 nanopore electrode was evaluated using high molecular weight organics (stearic acid) alongside with the photoconductivity. The successful degradation of stearic acid within hours suggests that the transparent TiO_2 nanopore electrode has potential to be useful for self-cleaning applications.

Acknowledgment. J. J. Zhu thanks the support from National Natural Science Foundation of China (20635020). H. G. Zheng thanks the support from National Natural Science Foundation of China (20971065). C. Burda thanks for partial support through NSF (#CHE-0239688).

REFERENCES AND NOTES

(1) Fujishima, A.; Honda, K. *Nature* **1972**, *238*, 37–38.
(2) Tryk, D. A.; Fujishima, A.; Honda, K. *Electrochim. Acta* **2000**, *45*, 2363–2376.
(3) Kraeutler, B.; Bard, A. J. *J. Am. Chem. Soc.* **1977**, *99*, 7729–7731.
(4) Joo, J.; Kwon, S. G.; Yu, T.; Cho, M.; Lee, J.; Yoon, J.; Hyeon, T. *J. Phys. Chem. B* **2005**, *109*, 15297–15302.
(5) Kikuchi, Y.; Sunada, K.; Iyoda, T.; Hashimoto, K.; Fujishima, A. *J. Photochem. Photobiol., A* **1997**, *106*, 51–56.
(6) Parkin, I. P.; Palgrave, R. G. *J. Mater. Chem.* **2005**, *15*, 1689–1695.
(7) Varghese, O. K.; Gong, D. W.; Paulose, M.; Ong, K. G.; Dickey, E. C.; Grimes, C. A. *Adv. Mater.* **2003**, *15*, 624–627.
(8) Ghicov, A.; Schmidt, B.; Kunze, J.; Schmuki, P. *Chem. Phys. Lett.* **2007**, *433*, 323–326.
(9) Paulose, M.; Shankar, K.; Varghese, O. K.; Mor, G. K.; Hardin, B.; Grimes, C. A. *Nanotechnology* **2006**, *17*, 1446–1448.
(10) Zhu, K.; Neale, N. R.; Miedaner, A.; Frank, A. J. *Nano Lett.* **2007**, *7*, 69–74.
(11) Li, S. Q.; Zhang, G. M.; Guo, D. Z.; Yu, L. G.; Zhang, W. *J. Phys. Chem. C* **2009**, *113*, 12759–12765.
(12) Liu, Z.; Zhang, X.; Nishimoto, S.; Jin, M.; Tryk, D. A.; Murakami, T.; Fujishima, A. *J. Phys. Chem. C* **2008**, *112*, 253–259.
(13) Yang, L. X.; Luo, S. L.; Liu, S. H.; Cai, Q. Y. *J. Phys. Chem. C* **2008**, *112*, 8939–8943.
(14) Sun, W. T.; Yu, Y.; Pan, H. Y.; Gao, X. F.; Chen, Q.; Peng, L. M. *J. Am. Chem. Soc.* **2008**, *130*, 1124–1125.
(15) Zhang, M.; Bando, Y.; Wada, K. *J. Mater. Sci. Lett.* **2001**, *20*, 167–170.
(16) Cai, Q. Y.; Paulose, M.; Varghese, O. K.; Grimes, C. A. *J. Mater. Res.* **2005**, *20*, 230–236.
(17) Zhu, Y. C.; Li, H. L.; Koltypin, Y.; Hacohen, Y. R.; Gedanken, A. *Chem. Commun.* **2001**, 2616–2617.
(18) Peng, T. Y.; Hasegawa, A.; Qiu, J. R.; Hirao, K. *Chem. Mater.* **2003**, *15*, 2011–2016.
(19) Zwilling, V.; Aucouturier, M.; Darque-Ceretti, E. *Electrochim. Acta* **1999**, *45*, 921–929.
(20) Gong, D.; Grimes, C. A.; Varghese, O. K.; Hu, W. C.; Singh, R. S.; Chen, Z.; Dickey, E. C. *J. Mater. Res.* **2001**, *16*, 3331–3334.
(21) Prakasam, H. E.; Shankar, K.; Paulose, M.; Varghese, O. K.; Grimes, C. A. *J. Phys. Chem. C* **2007**, *111*, 7235–7241.
(22) Paulose, M.; Shankar, K.; Yoriya, S.; Prakasam, H. E.; Varghese, O. K.; Mor, G. K.; Latempa, T. A.; Fitzgerald, A.; Grimes, C. A. *J. Phys. Chem. B* **2006**, *110*, 16179–16184.
(23) Macak, J. M.; Tsuchiya, H.; Schmuki, P. *Angew. Chem., Int. Ed.* **2005**, *44*, 2100–2102.
(24) Albu, S. R.; Kim, D.; Schmuki, P. *Angew. Chem., Int. Ed.* **2008**, *47*, 1916–1919.
(25) Wang, D. A.; Liu, Y.; Yu, B.; Zhou, F.; Liu, W. M. *Chem. Mater.* **2009**, *21*, 1198–1206.
(26) Yu, X. F.; Li, Y. X.; Ge, W. Y.; Yang, Q. B.; Zhu, N. F.; Kalantar-Zadeh, K. *Nanotechnol* **2006**, *17*, 808–814.
(27) Mor, G. K.; Varghese, O. K.; Paulose, M.; Grimes, C. A. *Adv. Funct. Mater.* **2005**, *15*, 1291–1296.
(28) Macak, J. M.; Tsuchiya, H.; Berger, S.; Bauer, S.; Fujimoto, S.; Schmuki, P. *Chem. Phys. Lett.* **2006**, *428*, 421–425.
(29) Yang, D. J.; Kim, H. G.; Cho, S. J.; Choi, W. Y. *Mater. Lett.* **2008**, *62*, 775–779.
(30) Wang, J.; Lin, Z. Q. *J. Phys. Chem. C* **2009**, *113*, 4026–4030.
(31) Mor, G. K.; Shankar, K.; Paulose, M.; Varghese, O. K.; Grimes, C. A. *Nano Lett.* **2006**, *6*, 215–218.
(32) Sadek, A. Z.; Zheng, H. D.; Latham, K.; Wlodarski, W.; Kalantar-Zadeh, K. *Langmuir* **2009**, *25*, 509–514.
(33) Berger, S.; Ghicov, A.; Nah, Y. C.; Schmuki, P. *Langmuir* **2009**, *25*, 4841–4844.
(34) Varghese, O. K.; Paulose, M.; Grimes, C. A. *Nat. Nanotechnol.* **2009**, *4*, 592–597.
(35) Yang, D. J.; Kim, H. G.; Cho, S. J.; Choi, W. Y. *IEEE Trans. Nanotechnol.* **2008**, *7*, 131–134.
(36) Kalantar-Zadeh, K.; Sadek, A. Z.; Zheng, H.; Partridge, J. G.; McCulloch, D. G.; Li, Y. X.; Yu, X. F.; Wlodarski, W. *Appl. Surf. Sci.* **2009**, *256*, 120–123.
(37) Varghese, O. K.; Gong, D. W.; Paulose, M.; Grimes, C. A.; Dickey, E. C. *J. Mater. Res.* **2003**, *18*, 156–165.

(38) Ghicov, A.; Alba, S. P.; Macak, J. M.; Schmuki, P. *Small* **2008**, *4*, 1063–1066.
(39) Bersani, D.; Antonioli, G.; Lottici, P. P.; Lopez, T. *J. Non-Cryst. Solids* **1998**, *232*, 175–181.
(40) Robert, T. D.; Laude, L. D.; Geskin, V. M.; Lazzaroni, R.; Gouttebaron, R. *Thin Solid Films* **2003**, *440*, 268–277.
(41) Wang, J.; Lin, Z. Q. *Chem. Mater.* **2008**, *20*, 1257–1261.
(42) Zhao, J. L.; Wang, X. H.; Chen, R. Z.; Li, L. T. *Solid State Commun.* **2005**, *134*, 705–7110.
(43) Kanai, N.; Nuida, T.; Ueta, K.; Hashimoto, K.; Watanabe, T.; Ohsaki, H. *Vacuum* **2004**, *74*, 723–727.
(44) Ohsaki, H.; Kanai, N.; Fukunaga, Y.; Suzuki, M.; Watanabe, T.; Hashimoto, K. *Thin Solid Films* **2006**, *502*, 138–142.
(45) Eppler, A. A.; Ballard, I. N.; Nelson, J. *Phys. E* **2002**, *14*, 197–202.
(46) Anpo, M.; Tomonari, M.; Fox, M. A. *J. Phys. Chem.* **1989**, *93*, 7300–7302.
(47) Golego, N.; Studenikin, S. A.; Cocivera, M. *Phys. Rev. B* **2000**, *61*, 8262–8269.
(48) Ohsaki, H.; Kanai, N.; Fukunaga, Y.; Suzuki, M.; Shibayama, Y.; Watanabe, T.; Hashimoto, K. *Thin Solid Films* **2008**, *516*, 4558–4562.
(49) Clouser, S.; Samia, A. C. S.; Navok, E.; Alred, J.; Burda, C. *Top. Catal.* **2008**, *47*, 42–48.
(50) Mor, G. K.; Varghese, O. K.; Paulose, M.; Mukherjee, N.; Grimes, C. A. *J. Mater. Res.* **2003**, *18*, 2588–2593.
(51) Taveira, L. V.; Macak, J. M.; Tsuchiya, H.; Dick, L. F. P.; Schmuki, P. *J. Electrochem. Soc.* **2005**, *152*, B405–B410.
(52) Minabe, T.; Tryk, D. A.; Sawunyama, P.; Kikuchi, Y.; Hashimoto, K.; Fujishima, A. *J. Photochem. Photobiol., A* **2000**, *137*, 53–62.
(53) Mills, A.; Lee, S. K.; Lepre, A.; Parkin, I. P.; O'Neill, S. A. *Photochem. Photobiol. Sci.* **2002**, *1*, 865–868.

AM100579G